Jet noise modelling and control / Modélisation et contrôle du bruit de jet

Global mode-based control of laminar and turbulent high-speed jets ☆

Mahesh Natarajan [a], Jonathan B. Freund [b], Daniel J. Bodony [a],*

[a] *Department of Aerospace Engineering, University of Illinois at Urbana–Champaign, Urbana, IL 61801, USA*
[b] *Department of Mechanical Science & Engineering and Department of Aerospace Engineering, University of Illinois at Urbana–Champaign, Urbana, IL 61801, USA*

A R T I C L E   I N F O

A B S T R A C T

The emitted noise from round jets is reduced using linear feedback controllers designed using structural sensitivity analysis. Linear global modes inform the selection and placement of the controller, and Navier–Stokes simulations are used to demonstrate effectiveness in a Mach-1.5 cold axisymmetric jet and in a Mach-0.9 cold turbulent jet. In both jets, each fitted with a cylindrical nozzle, the control reduces the radiated noise and modifies the baseflow in a way that enhances the relative amplitudes of low-frequency $St \approx 0.05$ global modes that do not have significant support in the acoustic field.

© 2018 Académie des sciences. Published by Elsevier Masson SAS. All rights reserved.

1. Introduction

Several decades of experimental, theoretical, and computational-based investigations have suggested that the basic structure of the loudest jet noise sound sources, i.e. those at low frequencies and radiating towards the downstream jet axis, are consistent with a wavepacket structure [1]. Different approaches have been used to describe these wavepackets, such as linear stability theory applied to spatially-developing shear layers and jets [2–9]. In jets, these wavepackets are intermittent, advecting disturbances that are correlated over distances that exceed the integral scales of turbulence [1]. Educing these structures from numerical or experimental data has, for example, included projecting the data onto locally-parallel instability waves [10] or parabolized stability equations (PSE, Gudmundsson and Colonius [11]), a process that can be augmented by using a proper orthogonal decomposition (POD) as a filter [12]. Numerically predicting the noise from the wavepackets modeled as instability waves has also been investigated by, for example, Balakumar [13], Yen and Messersmith [14], and Cheung et al. [15].

Global mode analysis complements these approaches in that it provides a direct means of analyzing the behavior of linear disturbances whose superposition can replicate a wavepacket character. Theofilis [16] and Theofilis and Colonius [17] review the use of global modes while Jordan and Colonius [1] review wavepackets as a model for low-frequency jet noise. Although they are more computationally intensive to compute than PSE modes, global modes are more faithful to the full

(a) Axisymmetric Mach-1.5 jet.
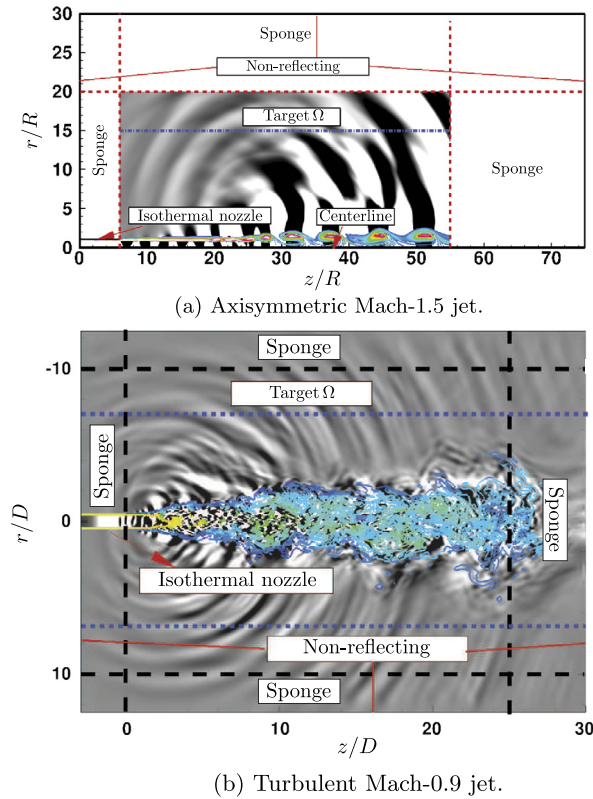

(b) Turbulent Mach-0.9 jet.

Fig. 1. Domain and boundary condition specifications for axisymmetric and turbulent jet calculations.

governing equations in that they do not invoke any spatial variation approximations of the flow field and, more importantly, allow for upstream–downstream coupling within the jet.

Several investigators examined the use of global modes to describe jet hydrodynamic and acoustic fields. Nichols and Lele [18], for example, used a global mode analysis about a parameterized baseflow to obtain the optimal transient response of a cold, supersonic jet and identified upstream-propagating acoustic modes that were not resolved in the earlier PSE analyses. Garnaud et al. [19] investigated the linear stability dynamics of incompressible and compressible isothermal jets by means of their optimal initial perturbations and of their global eigenmodes; see also Coenen et al. [20]. More recent investigations have focused on a resolvent analysis and determining optimal input–output gains for time-periodic disturbances (e.g., Semeraro et al. [21]).

In this paper we use global modes to control high-speed round jets using linear feedback. We include the nozzle in the simulations and analysis because it sets inflow conditions and couples flow disturbances. Moreover, the nozzle is the most natural platform for control of noise. We use the same numerical formulation to compute the adjoint global modes, which provide sensitivity via the wavemaker approach [22,23], and utilize it to develop the control. Adjoint global modes are key to assessing the importance of individual global modes in seeking quieter jets. Our control uses a structured sensitivity-based approach originally developed in Bodony and Natarajan [24] and subsequently expanded in Natarajan et al. [25].

We focus exclusively on the axisymmetric ($m = 0$) global modes because they are an important component of high-Reynolds-number turbulent jets [26], and thus an important testbed for control development. Jet noise control using higher order modes may be approached using the control method we develop without modification. We demonstrate the control first on an axisymmetric Mach-1.5 cold jet, followed by a turbulent Mach-0.9 cold jet that is axisymmetric in the mean.

The governing equations, numerical methods, boundary conditions, and the formulation and solution to the eigenvalue problems are discussed in Section 2. The results (simulation details, global mode analysis, and control) for the axisymmetric Mach-1.5 jet are given in Section 3. Section 4 gives the results corresponding to the cold Mach-0.9 turbulent jet. Following a discussion in Section 5, conclusions are drawn in Section 6.

2. Governing equations, boundary conditions, and numerical methods

The jets considered are shown in Fig. 1. The equations of mass, momentum, and energy conservation are solved for a compressible, viscous fluid with an ideal gas equation of state ($p = \rho R T$), Fourier law of heat conduction ($\mathbf{q} = -k\nabla T$) and Newtonian viscous stresses $\tau = \mu[\nabla\mathbf{u} + (\nabla\mathbf{u})^\mathsf{T}] + \lambda(\nabla \cdot \mathbf{u})\mathsf{I}$, where I is the identity tensor and $\mathbf{u}$ is the velocity field. For the axisymmetric jet the equations are expressed in cylindrical polar coordinates $\mathbf{x} = (r, \theta, z)$ using cylindrical polar velocities

$\boldsymbol{u} = \{V_r, V_\theta, V_z\}$. For the turbulent jet the equations utilize the Cartesian momentum densities expressed in computational coordinates $\boldsymbol{\xi} = \Xi(\boldsymbol{x})$ whose mapping to physical coordinates $\boldsymbol{x}$ is one-to-one and onto [27]. The ratio of specific heats $\gamma = C_p/C_v = 1.4$ and Prandtl number $Pr = \mu C_p/k = 0.72$ are constants representative of air at modest temperatures. The shear viscosity is temperature dependent as $\mu/\mu_{\text{ref}} = (T/T_{\text{ref}})^{2/3}$ and the second coefficient of viscosity is $\lambda = \mu_{\text{B}} - (2/3)\mu$, where $\mu_{\text{B}} = 0.6\mu$ is the bulk viscosity.

2.1. Boundary conditions

The computational domain and supporting boundary conditions for the axisymmetric Mach-1.5 jet and the three-dimensional, axisymmetric in-the-mean Mach-0.9 jet, are very similar and jointly described in this section. Fig. 1 shows the domains and boundary conditions used in the jet simulations. Both jets issue from constant area isothermal nozzles with constant upstream stagnation conditions. The nozzle thickness is a constant $0.05\,R$ and the wall temperature is equal to the ambient temperature. All upstream, downstream, and lateral boundaries are non-reflecting while the nozzle is isothermal with no-slip walls. An additional boundary treatment using sponge zones [28,29] surrounds all boundaries to further reduce unwanted reflections and better impose constant stagnation conditions. The reference solution in the sponge zone was computed using an auxiliary computation of the corresponding jet at the same conditions but on a larger domain. For the axisymmetric jet only, the $r = 0$ centerline (see Fig. 1(a)) uses the polar axis treatment of Lewis and Bellan [30] (also see Natarajan [31]). The flow into the nozzle has laminar boundary layers with a specified momentum thickness, the details of which are given in the Results section for each jet.

2.2. Numerical discretization

The axisymmetric and turbulent jets utilize similar numerical methods, albeit with a difference in the treatment of the viscous terms. A collocated finite difference approximation is used where the spatial derivatives are approximated by diagonal norm summation-by-parts (SBP) operators that are fourth order in the interior, second order at boundaries, and globally third order [32]. The Mach-0.9 jet solves the filtered (LES) equations and uses a standard dynamic Smagorinsky model formulated for a compressible fluid [33] with Lilly's improvement [34] using a 7-point explicit least squares test filter [35]. The flow solution is also filtered using a tridiagonal implicit filter with $\alpha_{\text{f}} = 0.49$ [36]. The turbulent jet uses repeated first derivatives to approximate the divergence of the molecular and LES-informed transport fluxes and the 10th-order high-wavenumber filter of Visbal and Gaitonde [27] with free parameter $\alpha_{\text{f}} = 0.49$ to suppress numerical instabilities caused by the wide stencil approximation to the viscous terms. In contrast, the axisymmetric jet uses narrow stencil second derivative operators and the expanded form of the viscous terms. The weak shocks present in the Mach-1.5 jet are captured using the artificial transport property method described in Kawai et al. [37]. Implementation of the boundary conditions shown in Fig. 1 uses the simultaneous-approximation-term (SAT) approach [38–40] which has been shown to be accurate and stable for aeroacoustic calculations [41]. The discrete system of coupled, nonlinear ordinary differential equations is integrated in time using the standard fourth-order Runge–Kutta method.

2.3. Global eigenvalue problem

2.3.1. Forward eigenvalue problem

The discretized flow equations may be written as

$$\frac{\text{d}\boldsymbol{Q}}{\text{d}t} = \tilde{\boldsymbol{R}}(\boldsymbol{Q}) \tag{1}$$

where $\boldsymbol{Q}$ is the vector of unknowns and $\tilde{\boldsymbol{R}}$ is the discretized right-hand side, including the SAT, sponges, and the LES or artificial viscosity terms. Linearization of Eq. (1) for small perturbation $\boldsymbol{Q}'$ to baseflow $\bar{\boldsymbol{Q}}$ yields

$$\frac{\text{d}\boldsymbol{Q}'}{\text{d}t} = \boldsymbol{L}(\bar{\boldsymbol{Q}})\boldsymbol{Q}' \tag{2}$$

where $\boldsymbol{L}$ is the discrete right hand side operator evaluated about the axisymmetric baseflow $\bar{\boldsymbol{Q}}$. The eigenvalue problem we consider is based on a modal decomposition of the form

$$\boldsymbol{Q}' = \hat{\boldsymbol{Q}}(r, z)\text{e}^{im\theta + \omega t} \tag{3}$$

where m is the specified azimuthal mode number and ω is the sought-after eigenvalue with eigenmode $\hat{\boldsymbol{Q}}$. The boundary conditions convert Eq. (2) to the generalized eigenvalue problem

$$\boldsymbol{L}\hat{Q} = \omega\boldsymbol{M}\hat{Q} \tag{4}$$

The axis conditions are either Dirichlet or Neumann such that $\boldsymbol{M}$ is a diagonal matrix that has an entry 0 for all rows corresponding to the axis (with a corresponding diagonal entry of 1 in $\boldsymbol{L}$), and an entry 1 for all the remaining rows [31]. Both the axisymmetric Mach-1.5 jet and the axisymmetric in-the-mean Mach-0.9 jet use the same eigenvalue solver.

Table 1

Simulation parameters for the axisymmetric jet.

Domain size	$(L_z, L_r) = (60R, 30R)$
Grid points	$(N_z, N_r) = (4400, 640)$
Nozzle length	$L_{\text{nozzle}}/R = 6$
Nozzle thickness	$t_{\text{nozzle}}/R = 0.05$
Reynolds number	$\rho_j U_j D/\mu_j = 10{,}885$
Mach number	$U_j/c_j = 1.5$
Temperature ratio	$T_j/T_\infty = 0.6$
Nozzle wall temperature	$T_{\text{w}}/T_\infty = 1$
Momentum thickness at nozzle exit	$\theta/R = 0.01$
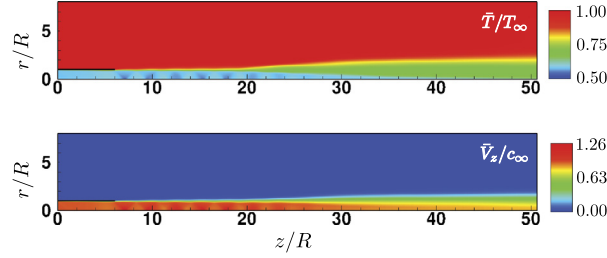
Fig. 2. Mean flow for the Mach-1.5 axisymmetric jet: top, temperature; bottom, axial velocity.

2.3.2. Adjoint eigenvalue problem

We use a volume-corrected formulation [42] to obtain the discrete adjoint eigenvalue problem. Multiplying Eq. (4) by $\hat{\boldsymbol{Q}}^\dagger \boldsymbol{D}$, where $\hat{\boldsymbol{Q}}^\dagger$ is the adjoint eigenmode and $\boldsymbol{D} = \text{diag}(v_1/V, v_2/V, \ldots, v_n/V)$ is a diagonal matrix in which V is the volume of the domain and v_i is the volume associated with the ith grid point, yields

$$(\boldsymbol{L}^{\text{H}} \boldsymbol{D}^{\text{H}} \hat{\boldsymbol{Q}}^\dagger)^{\text{H}} \hat{\boldsymbol{Q}} = (\boldsymbol{M}^{\text{H}} \omega^* \boldsymbol{D}^{\text{H}} \hat{\boldsymbol{Q}}^\dagger)^{\text{H}} \hat{\boldsymbol{Q}} \tag{5}$$

where the superscript 'H' denotes a complex conjugate transpose. Since Eq. (5) holds for arbitrary $\hat{\boldsymbol{Q}}$, the discrete adjoint eigenvalue problem is

$$\boldsymbol{L}^{\text{H}} \boldsymbol{D} \hat{\boldsymbol{Q}}^\dagger = \omega^* \boldsymbol{M}^{\text{H}} \boldsymbol{D} \hat{\boldsymbol{Q}}^\dagger \tag{6}$$

The eigenspectrum for the discrete adjoint problem is the same as the forward problem; however, the eigenvectors of the adjoint system differ.

2.3.3. Eigenvalue solver

The eigenvalue solver for the forward and adjoint systems (Eqs. (4) and (6), respectively) uses PETSc [43–45] for the matrix construction and SLEPc [46] to solve the global eigenvalue problem. The Krylov–Schur implementation of the Implicitly Restarted Arnoldi Method (IRAM), with MUMPS [47] for the LU factorization of the linearized Navier–Stokes operator, is used to obtain the eigenvalues that are closest to a specified target in absolute value in the complex plane and the corresponding eigenmodes.

3. Axisymmetric Mach-1.5 cold jet

To present ideas we focus first on the simpler axisymmetric Mach-1.5 cold jet. After presenting the jet's mean flow, we develop the controller and apply it to reduce the jet's transient growth as a sound generation mechanism, easily describable by global modes, and demonstrate noise reduction.

3.1. Flow solution

The simulation parameters are given in Table 1. The stretched and orthogonal computational grid used $(N_z, N_r) = (4400, 640)$ points in the axial and radial directions, respectively, and was shown to be sufficiently refined in Natarajan [31]. The flow simulations provide a time-average solution $\bar{\boldsymbol{Q}}$. The equilibrium baseflow solution, which satisfies $\tilde{\boldsymbol{R}}(\boldsymbol{Q}_e) = 0$ and computed using the method of Åkervik et al. [48], was used as the initial condition for a time-resolved calculation, which was averaged over a period of $\Delta t c_\infty/R \sim 600$ to obtain $\bar{\boldsymbol{Q}}$. Fig. 2 shows the contours of the time-averaged axial velocity and temperature. Details of the equilibrium solution, and its global mode analysis, may be found in [31].

3.2. Global mode analysis

To construct and solve the eigenvalue problems (Eqs. (4) and (6)) the time-averaged baseflow was linearly interpolated onto a mesh of size $(N_z, N_r) = (1100, 300)$ which was shown in Natarajan [31] to ensure mesh insensitivity to our quantities of interest. The time-average flow was chosen as the base state because past work has shown that linear analysis applied to it yield superior estimates of the frequencies of the unsteady modes [49,50]. Target eigenvalues $(\omega_{r\,\text{target}}, St_{\text{target}})$ (marked 'x' in Fig. 3) were used with $\omega_{r\,\text{target}} = 0.00$ and St_{target} in the range of 0.05–0.65, with a spacing of $\triangle St_{\text{target}} = 0.05$. For each target eigenvalue, 30 eigenmodes were obtained using the convergence criterion $||\boldsymbol{L}\,\hat{\boldsymbol{Q}} - \omega\boldsymbol{M}\,\hat{\boldsymbol{Q}}\,||/||\omega\boldsymbol{M}\,\hat{\boldsymbol{Q}}\,|| \sim 10^{-10}$.

Fig. 3 shows the globally stable eigenspectrum of the time-averaged baseflow $\bar{\boldsymbol{Q}}$. The time-average flow supports downstream-propagating (type A) and upstream-propagating (type B) modes [18]. Figs. 3(b–e) show the type-A modes for eigenvalues at different Strouhal numbers (A_1^t–A_4^t). These modes have a predominantly downstream-propagating wavepacket structure with a strong acoustic footprint, which supports a connection to the far-field noise radiation. Figs. 3(f–g) show type B modes. Unlike type-A modes, these modes have a strong upstream-propagating component. Type A and B modes were studied by Nichols and Lele [18]. The spectrum also contains hydrodynamically bound modes, identified as $H_{1,2}^t$ in Figs. 3(h–i) which are acoustically inefficient. We call these modes type H and will find them to be important for reducing the jet noise.

A spatial overlap of the forward–adjoint pair corresponding to a given eigenvalue defines a localized region in space called the wavemaker wherein the eigenspectrum is most sensitive to modifications of the baseflow [22]. Following Giannetti and Luchini [23], the wavemaker is

$$\mathcal{W}(z, r) = \frac{(\hat{\boldsymbol{Q}}^{\dagger})^{\mathsf{T}} \boldsymbol{D} \delta\boldsymbol{L}\,\hat{\boldsymbol{Q}}}{(\hat{\boldsymbol{Q}}^{\dagger})^{\mathsf{T}} \boldsymbol{M}\,\hat{\boldsymbol{Q}}} \tag{7}$$

where $\delta\boldsymbol{L}$ is the perturbation to the linearized operator $\boldsymbol{L}$. For a case with $\delta\boldsymbol{L}$ equal to the identity, the wavemaker region for the forward–adjoint pairs corresponding to the eigenvalues A_1^t through A_4^t are shown in Fig. 4. Peak values of the wavemaker close to the nozzle lip indicates high dynamical sensitivity to localized changes in the baseflow and suggest that the nozzle lip is a profitable location for feedback control, as has been widely recognized.

3.3. Optimal transient growth

As a consequence of the non-normality of the linearized operator, for a globally stable system it is possible to obtain perturbation growth for a finite period of time by a particular superposition of the global modes [51]. Optimal transient growth represents the worst case scenario for the linear system in terms of the amplification of the defined disturbance energy norm. Since the motivation of this work is noise control, a pressure perturbation based energy semi-norm defined as

$$E(t) = \frac{1}{2} \int_{\Omega} \hat{p}(t)\hat{p}(t)^* \, \mathrm{d}V = \frac{1}{2} \int_{\Omega} \hat{p}(t)\hat{p}(t)^* \, r \, \mathrm{d}r \, \mathrm{d}z \tag{8}$$

where Ω is the target surface shown in Fig. 1, would be instructive as an alternative to the energy-based norm used by Nichols and Lele [18]. Optimal transient growth is the envelope of the worst case scenario for all t and is given by

$$G(t) = \max \frac{\left\| \boldsymbol{Q}(t) \right\|_E^2}{\left\| \boldsymbol{Q}(0) \right\|_E^2} \tag{9}$$

where $\boldsymbol{Q}(0)$ and $\boldsymbol{Q}(t)$ are the initial condition and its response, respectively. A singular-value decomposition problem is formulated to solve for $G(t)$, and the optimal initial condition $\boldsymbol{Q}_{\text{opt}}(0)$ to obtain the transient response at any given time t can be computed [52,31]. Fig. 5(a) shows the optimal transient response envelope for the eigenspectrum of the time-averaged baseflow for $m = 0$ and $m = 1$ modes. From the transient response analysis, we can arrange the global modes in order of prominence of their contribution to the initial condition that achieves the maximum transient growth amplification as shown in Figs. 5(b) and (c), respectively. The size of the circle surrounding the symbols is proportional to the contribution of the corresponding global mode to the optimal initial condition [31]. It is observed that the optimal transient response is predominantly due to the superposition of type A global modes in the frequency range $St \sim 0.45$–0.65. The optimal transient growth is associated with a propagating aerodynamic wavepacket which emits an acoustic wavepacket into the far field (Figs. 5(d)–(i)), which is a potential mechanism for jet noise production and propagation (Nichols and Lele [18]), as well as a control objective.

3.4. Linear feedback control

We control the jet by designing a linear feedback controller selected to optimally move the eigenmode that most contributes to the transient growth of the Mach-1.5 jet. How the control is designed is described prior to demonstrating its effect on the jet.
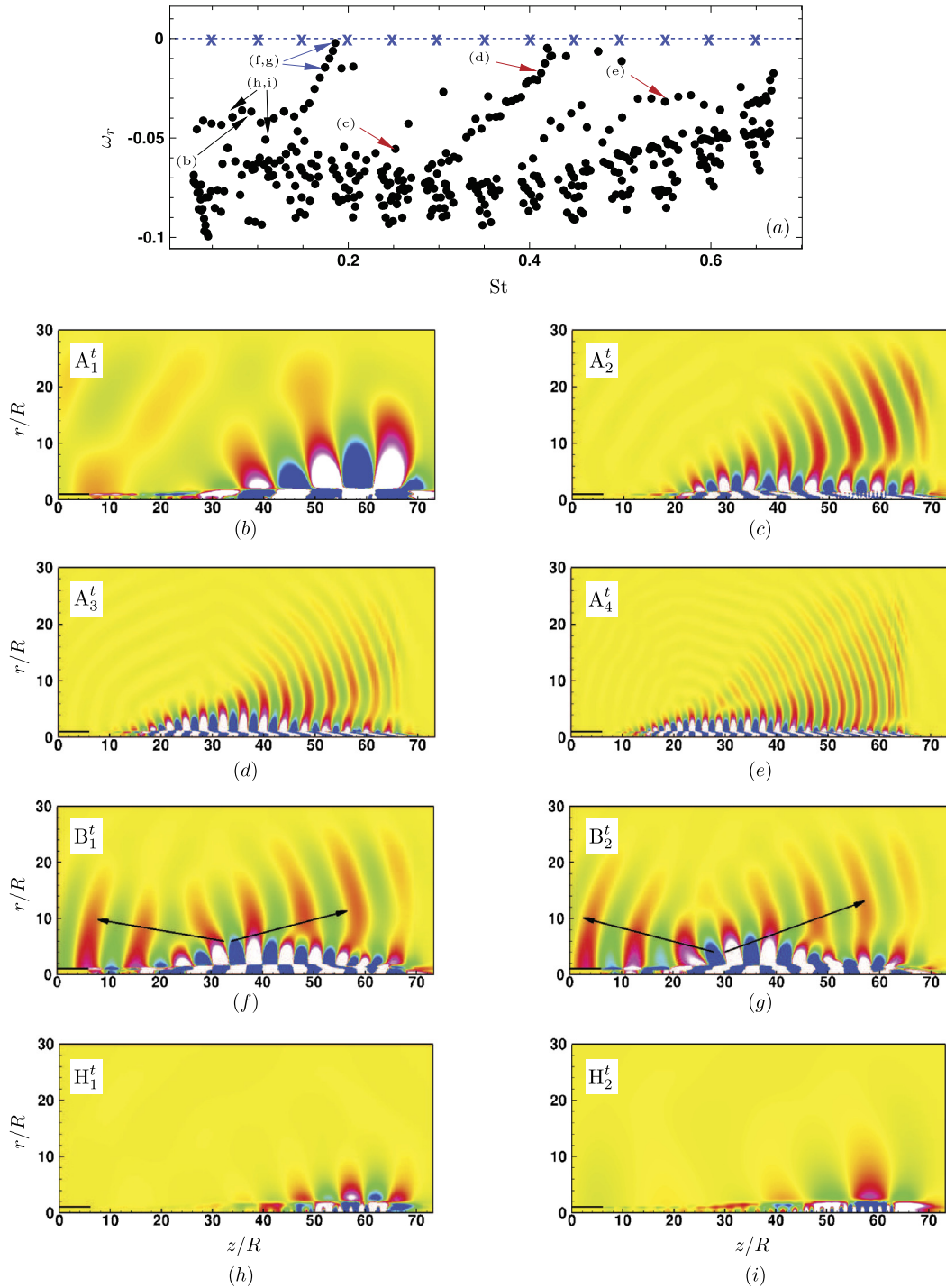
Fig. 3. Global modes of the time-averaged $\bar{\boldsymbol{Q}}$: (a) eigenspectrum; forward global modes ($\text{Re}\{\hat{V}_z\}$) of type-A modes (downstream-propagating): (b) A_1^t (c) A_2^t (d) A_3^t, and (e) A_4^t; type B modes (with a predominant upstream-propagating wave structure): (f) B_1^t (g) B_2^t; Hydrodynamic type H modes (h) H_1^t (i) H_2^t. The parenthetical letters in subfigure (a) refer to the corresponding subfigure in which that mode is shown. The contours have min/max values of $\hat{V}_z/c_\infty$ of $\pm 10^{-4}$.

3.4.1. Controller selection

The framework developed in Natarajan et al. [25] for the global eigenanalysis is utilized to develop a control strategy using co-located linear feedback, where the feedback sensing is based on the difference between the instantaneous value of the flow variable from that of the baseflow which, for our case, is the uncontrolled time-average. The Navier–Stokes
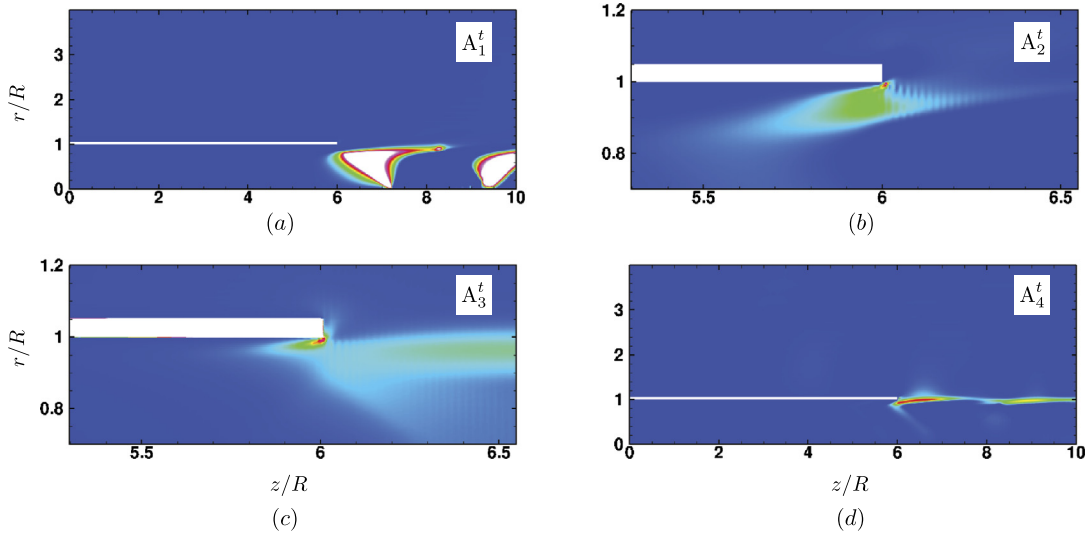
Fig. 4. Wavemaker region $\mathcal{W}(z,r)$ defined by Eq. (7) for modes: (a) A_1^t (b) A_2^t (c) A_3^t (d) A_4^t. Contours levels are between 0 and 0.01.

equation with the control forcing terms is given by

$$\frac{\mathrm{d}\mathbf{Q}}{\mathrm{d}t} = \tilde{\mathbf{R}}(\mathbf{Q}) + \underbrace{\alpha\mathbf{C}(\mathbf{Q} - \bar{\mathbf{Q}})}_{\text{Forcing } \mathbf{F}(\mathbf{x},t)} \tag{10}$$

where α is the control gain and $\mathbf{C}$ is a control matrix designed to best alter the eigensystem of the linearized operator. $\mathbf{C}$ is a 5×5 matrix for three-dimensional problems. The entries of $\mathbf{C}$ identify sensor–actuator pairs and localize the actuator–sensor pair, as

$$\mathbf{C} = \underbrace{\begin{bmatrix} \tilde{c}_{1,1} & \tilde{c}_{1,2} & \tilde{c}_{1,3} & \tilde{c}_{1,4} & \tilde{c}_{1,5} \\ \tilde{c}_{2,1} & \tilde{c}_{2,2} & \tilde{c}_{2,3} & \tilde{c}_{2,4} & \tilde{c}_{2,5} \\ \tilde{c}_{3,1} & \tilde{c}_{3,2} & \tilde{c}_{3,3} & \tilde{c}_{3,4} & \tilde{c}_{3,5} \\ \tilde{c}_{4,1} & \tilde{c}_{4,2} & \tilde{c}_{4,3} & \tilde{c}_{4,4} & \tilde{c}_{4,5} \\ \tilde{c}_{5,1} & \tilde{c}_{5,2} & \tilde{c}_{5,3} & \tilde{c}_{5,4} & \tilde{c}_{5,5} \end{bmatrix}}_{\tilde{c}} \mathrm{e}^{-(z-z_0)^2/\ell_z^2 - (r-r_0)^2/\ell_r^2} \tag{11}$$

where (z_0, r_0) is the center of the actuator and (ℓ_z, ℓ_r) is the support in the z and r directions respectively. For this linear system, the control gain α is a free parameter that can be varied to change the strength of the control. A discrete structural sensitivity analysis [25] gives the eigenspectrum shift due to the control as

$$\delta\omega = \frac{(\hat{\mathbf{Q}}^\dagger)^{\mathsf{T}}\mathbf{D}\mathbf{C}\,\hat{\mathbf{Q}}}{(\hat{\mathbf{Q}}^\dagger)^{\mathsf{T}}\mathbf{M}\hat{\mathbf{Q}}} \tag{12}$$

The objective we pursue is to optimize the movement of the chosen target eigenvalue to reduce transient growth. The optimization seeks

$$\mathbf{C}^* \stackrel{\text{def}}{=} \underset{\mathbf{C},\|\tilde{c}\|=1}{\mathrm{argmin}} \, \mathrm{Re}(\alpha^{-1}\delta\omega) \tag{13}$$

with respect to the parameters $\{\{c_{ij}\}_{i,j=1}^5, z_0, r_0, \ell_z, \ell_r\}$. The optimization is performed using the Trust-Region-Reflective algorithm [53]. More details on the use of structural sensitivity to design and locate controllers can be found in Natarajan et al. [25] and Natarajan [31]. A flow chart of the control strategy is shown in Fig. 6. An important feature of the optimization problem is that it is computationally tractable with 31 parameters for a three-dimensional problem. Our experience is that the optimization requires around 10–15 minutes of time on a single processor.

3.4.2. Controller development

With the hypothesis that modifying the transient growth process will disrupt the jet's radiated noise we determine the optimal control matrix $\mathbf{C}^*$ that most stabilizes the target eigenmode shown in Fig. 5(b). Our use of transient growth
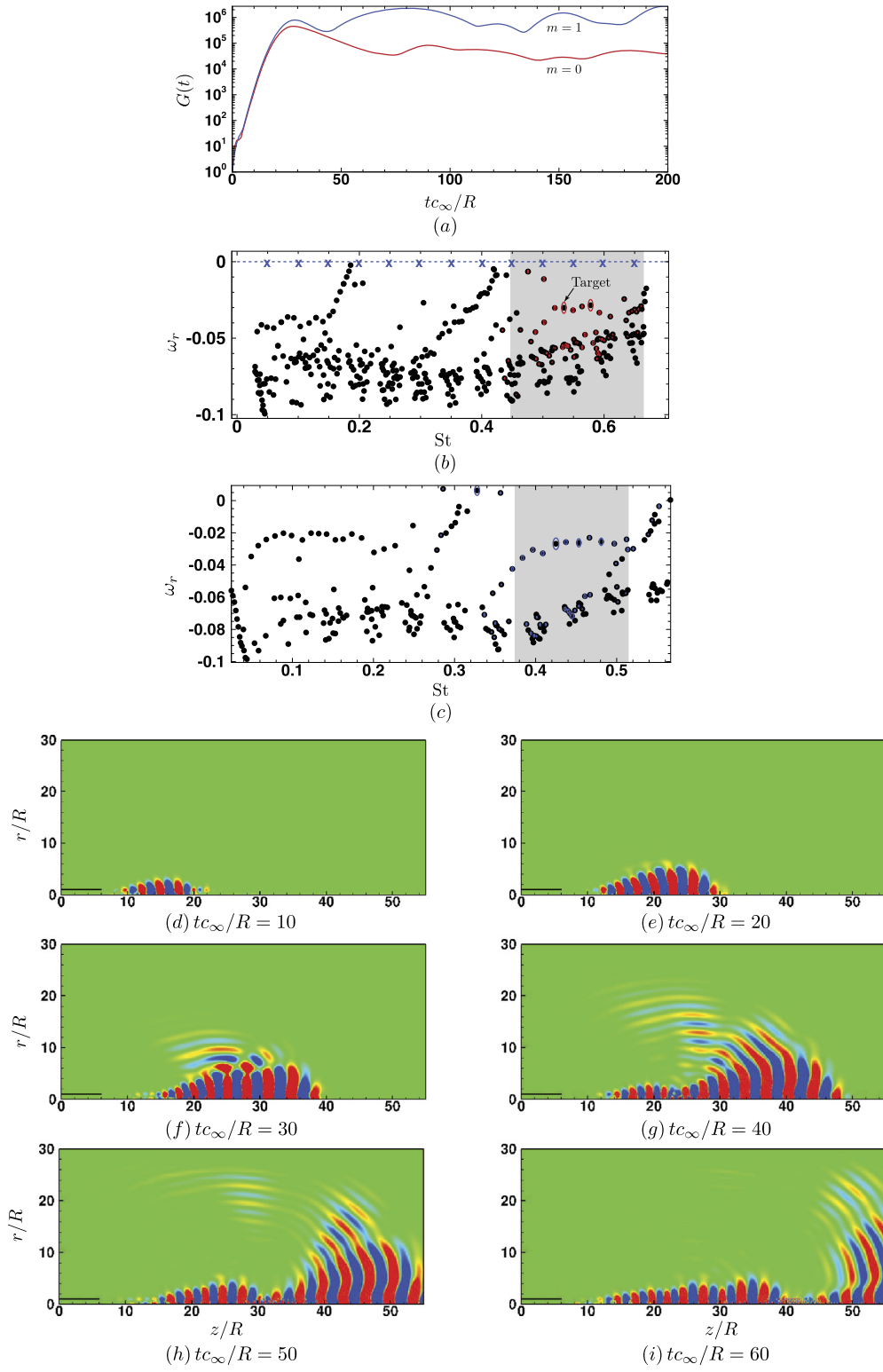
Fig. 5. (a) Optimal transient response for the time-averaged baseflow for $m = 0$ (—) and $m = 1$ (—) modes; Mode contribution to the optimal initial condition for (b) $m = 0$ (c) $m = 1$. The size of the circle surrounding the symbols is proportional to the contribution of the corresponding global mode to the optimal initial condition. Figures (d)–(i) show the evolution of the $m = 0$ optimal initial condition. Color levels in (d)–(i) show the real part of perturbation pressure with min/max values of ± 0.5.
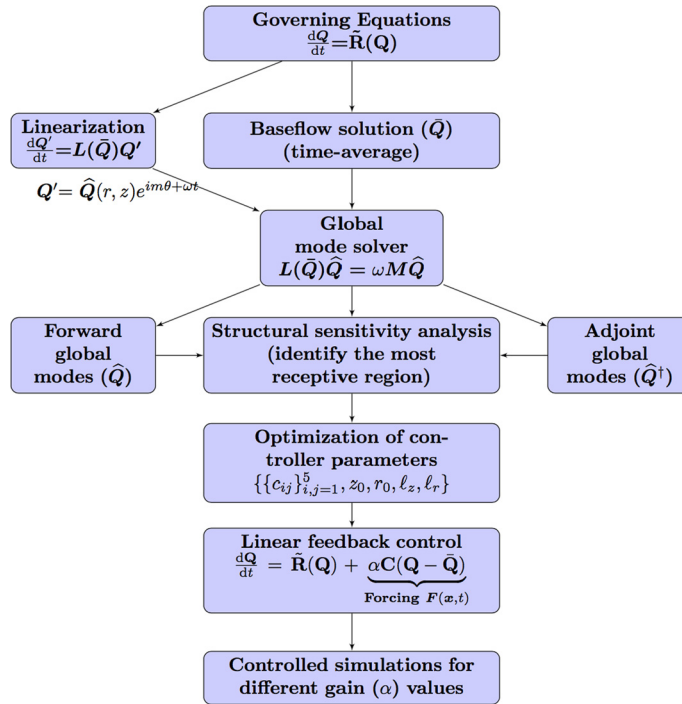
Fig. 6. Flow chart of the control strategy.
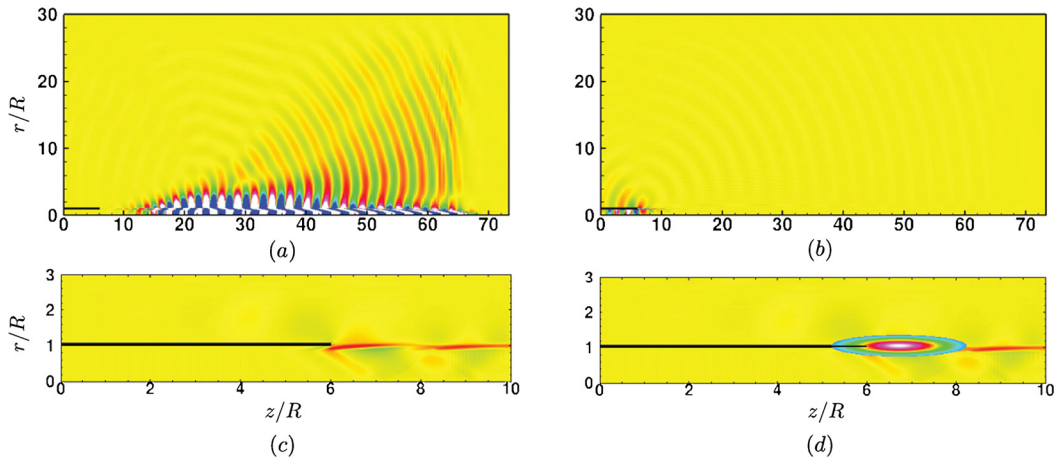
Fig. 7. Visualization of the (a) flow eigenmode ($\hat{V}_z$), (b) adjoint eigenmode ($\hat{V}_z^\dagger$), (c) wavemaker, and (d) the co-located actuator/sensor region for V_z–V_r control-feedback. Contour levels for (a) and (b) are between $\pm 2.5 \times 10^{-4}$ while (c) and (d) are between 0 and 1.

as the physical connection between the global modes at the jet's radiated sound is not unique but is informed by experimental and simulation evidence (Jordan and Colonius [1]). From the optimal transient response analysis, the eigenvalue that contributes most to the optimal initial condition is chosen as the target eigenmode. The optimal parameters $\{\{c_{ij}\}_{i,j=1}^5, z_0, r_0, \ell_z, \ell_r\}$ were found using the optimization procedure described in Section 3.4.1 for the forward and adjoint global modes shown in Fig. 7(a–b). A single variable control-single variable feedback control strategy is adopted. The optimization problem of Eq. (13) was performed, and it was found that the best control, as defined as being able to effectively stabilize the target eigenvalue, yields a $\tilde{C}^*$ that senses the radial velocity and forces the axial momentum just downstream and outside the nozzle as shown in Fig. 7(d). The optimal location and size parameters were found to be $(r_0^*, z_0^*, \ell_r^*, \ell_z^*) = (1.05, 6.72, 0.19, 0.98)R$. Observe that the best controller lies close to the wavemaker (Fig. 7(c)) but has localized support and uses specific quantities to control and sense. The location and size of the controller in the axial and radial directions were found as part of the optimization process and were not specified. More details on the controller selection process can be found in Natarajan [31].

Table 2
Direct numerical simulations to study the effect of control on far-field sound.

Simulation	Control gain (α)	Effect on far-field noise
Flow L1	0.0	Uncontrolled flow
Flow L2	2.0	Quieter
Flow L3	4.0	Quieter
Flow L4	−2.0	Louder
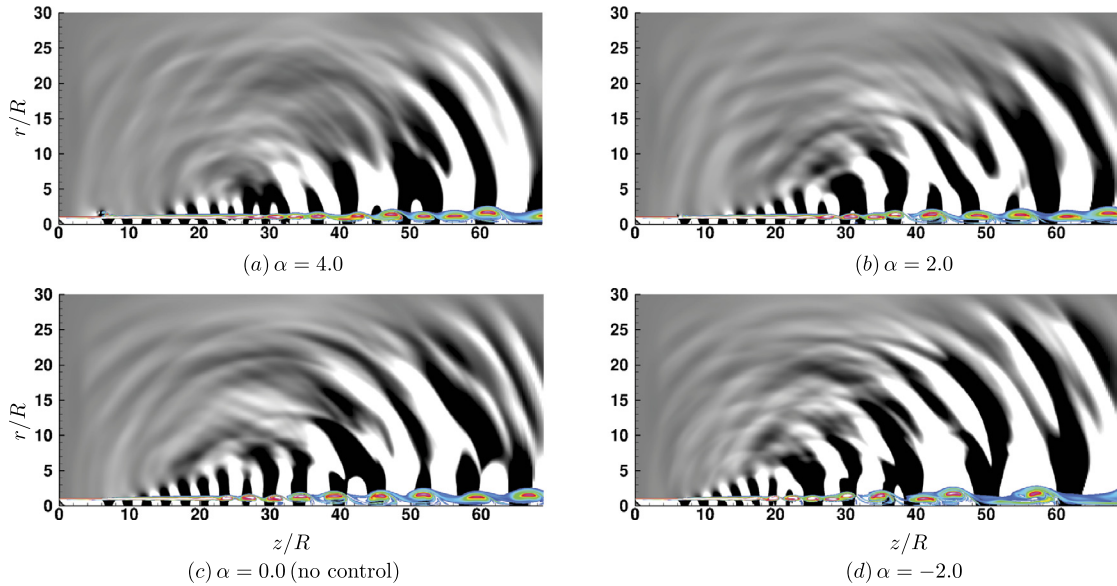
Fig. 8. Contour plot of vorticity magnitude ($0 \leq |\omega R/c_\infty| \leq 3$) and pressure perturbation ($|p - p_\infty|/(\rho_\infty c_\infty^2) \leq 2.5 \times 10^{-4}$) at $tc_\infty/R = 870$: (a) $\alpha = 4.0$, (b) $\alpha = 2.0$, (c) no control, and (d) $\alpha = -2.0$.

3.4.3. Controlled jet simulations

To assess the performance of the control on the far-field sound of the baseline jet (denoted flow L1), nonlinear simulations were carried out with the controller developed in Section 3.4.2 with three different gains: flow L2 with $\alpha = 2.0$, flow L3 with $\alpha = 4.0$ and flow L4 with $\alpha = -2.0$. Table 2 summarizes the flows and their far-field noise relative to the uncontrolled flow. Note that flow L4, with $\alpha = -2.0$, applies the controller such that the target mode is destabilized, rather than stabilized.

The target surface to quantify the radiated noise is a cylindrical region Ω at $r/R = 15$ (Fig. 1(a)) and the measurement function is

$$\mathcal{I}(t) = \int_\Omega (p(t) - \bar{p})^2 \, \mathrm{d}\Omega \tag{14}$$

Fig. 8 shows the contours of vorticity and pressure perturbation at time $tc_\infty/R = 870$ for all the cases in Table 2. The pressure perturbation contours clearly suggest the radiated sound is higher for Flow L4, the case for which the control destabilizes, rather than stabilizes, the target eigenmode. Fig. 9 shows an instantaneous snapshot of vorticity for all the cases. For the quieter flows L2 and L3, the vortex pairing is less vigorous and is delayed further downstream by the control, a conclusion confirmed in the Reynolds stresses (Fig. 10) where the peak values are reduced with favorable control and monotonicity is increased in the jet development region, $z/R \lesssim 25$. Fig. 11 shows the corresponding measurement function $\mathcal{I}(t)$ for all the flows of Table 2 where we observe that increasing the gain in the direction of mode stabilization reduces the jet's radiated noise. The trend can be observed in Fig. 11(b) as well, which shows the overall sound pressure level (OASPL) along the target surface Ω.

3.4.4. Global eigenanalysis of controlled flows

We apply the global mode analysis to the controlled jets and seek to understand what dynamical changes the control induced into the jet. We start by performing a global mode analysis on the time-averaged controlled flows (L2–L4 in Table 2) and comparing the resulting spectra and modes to the uncontrolled case (flow L1). Fig. 12 shows the controlled jet spectra around the target eigenvalue while Fig. 13 shows the resulting spectra with emphasis given in the low-frequency range
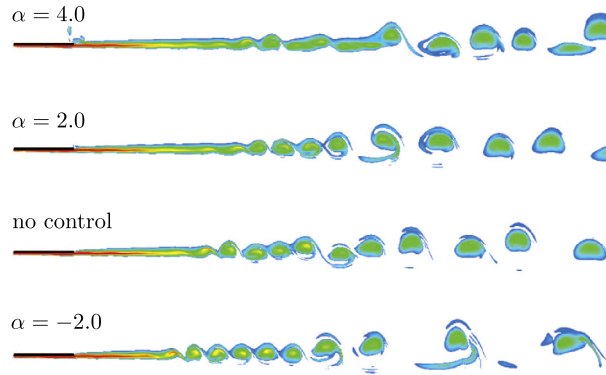
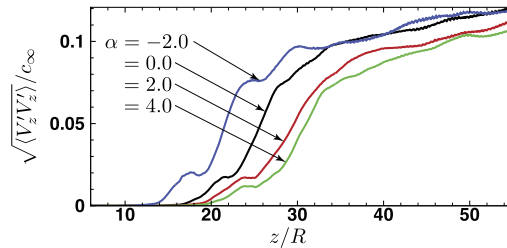**Fig. 9.** Visualization with vorticity at $t c_\infty/R = 880$.

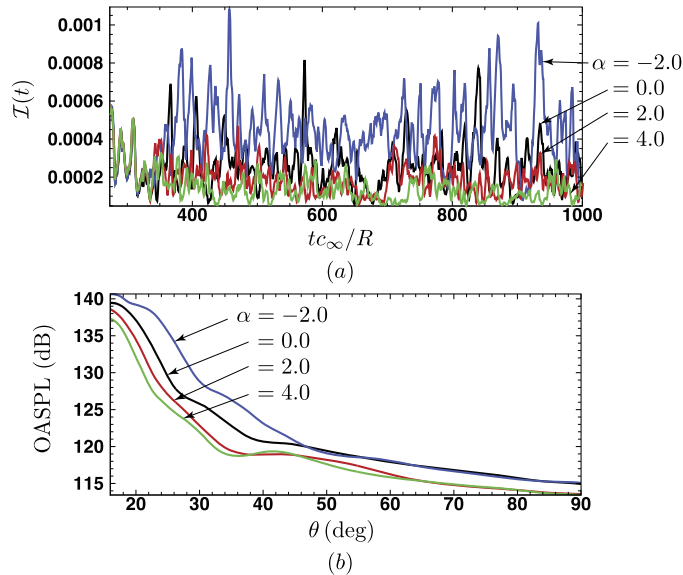**Fig. 10.** Effect of control on the lipline ($r/R = 1$) root-mean-square axial velocity fluctuations.

Fig. 11. (a) The measurement function $\mathcal{I}(t)$ at $r/R = 15$: —— uncontrolled; —— $\alpha = 2.0$; —— $\alpha = 4.0$; —— $\alpha = -2.0$; (b) the overall sound pressure level on target surface Ω (θ is the angle measured from the jet axis with the vertex at the nozzle exit).

of $St < 0.13$ (compare to Fig. 5(b)). As the gain α increased, the controlled jet spectrum changed from its uncontrolled jet spectrum. The target eigenvalues contributing to the transient growth are moved, as shown in Fig. 12. Observe that although the optimization sought to stabilize the eigenvalues, the ultimate change in the spectrum was a combination of stabilization and modest increase in frequency by $\Delta St \approx 0.005$. There is also an important and clear change for the very-low-frequency modes shown in Fig. 13 with the appearance of a single, unstable mode of frequency $St \approx 0.06$ whose growth rate ω_r increases with increasing α. It is noteworthy that the unstable eigenvalue appears only when the control acts to reduce the noise, rather than increase it. The unstable eigenvalue will ultimately dominate the transient growth response of the controlled jet on timescales of the order $T c_\infty/R = 2/(St\, U_j/c_\infty) \approx 30$ and is thus not shown.

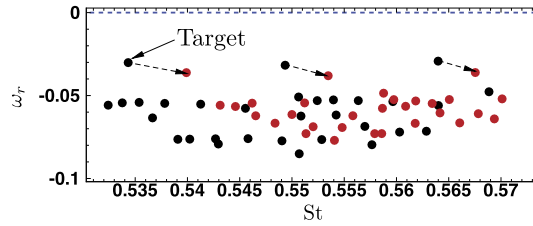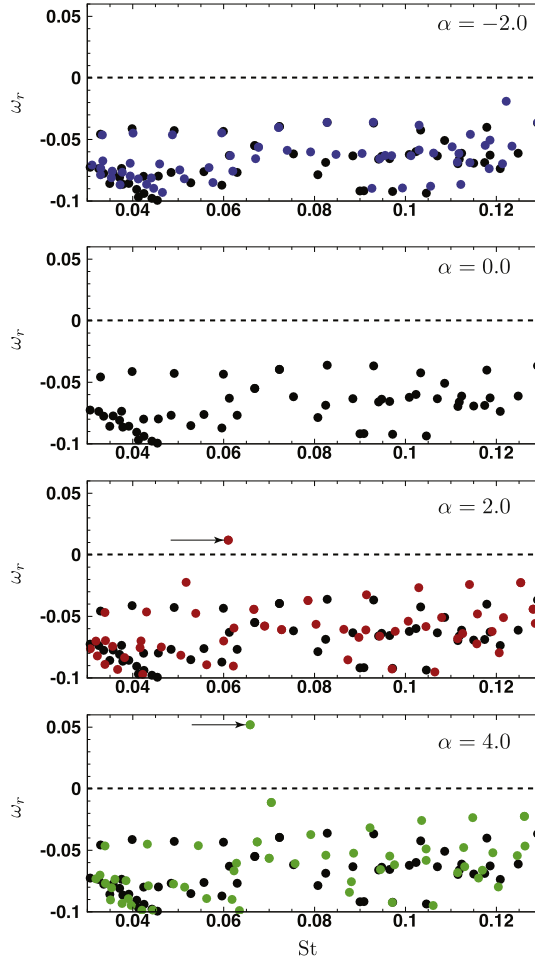**Fig. 12.** Movement of jet global mode spectrum from uncontrolled (●) to controlled (●) for $\alpha = 4.0$.

Fig. 13. Eigenspectra for all time-averaged flows: ● uncontrolled, ● $\alpha = 2.0$, ● $\alpha = 4.0$, and ● $\alpha = -2.0$. The spectrum without control is shown in each panel.

More interesting is the mode shape associated with the unstable eigenvalue, shown in Fig. 14, which has a strong resemblance to the $H_{1,2}^t$ modes discussed earlier (see Fig. 3). The unstable global modes are characterized by a hydrodynamic field with a relatively weak acoustic field; they are hydrodynamically bound to the jet.

The importance of these modes is apparent in Fig. 15 where we project the unsteady data $\mathbf{Q}' = \mathbf{Q} - \overline{\mathbf{Q}}$ onto the global modes, $\mathbf{Q}' = \sum_m c_m(t) \hat{\mathbf{Q}}_m$, using the biorthogonality of the forward and adjoint eigenvector pair. It is observed that in flows L1 and L4, the baseline and louder controlled jet, no individual mode dominates the perturbation field. In contrast, for the quieter jets (L2 and L3), the unstable mode prominently appears with coefficient amplitudes at least $10\times$ greater than all other modes. It can be seen that the unstable modes have a much higher amplification, reach a limit cycle and continue to be more prominent in the flow field throughout the control time period. Hence the unstable modes, which do not have any significant acoustic footprint, are more prominent in the flow field than the acoustically efficient stable modes.

These results suggest that the control, which was developed to affect the transient growth mechanism with central Strouhal number around 0.5, creates a new baseflow on which a single unstable mode exists and which becomes dynami-
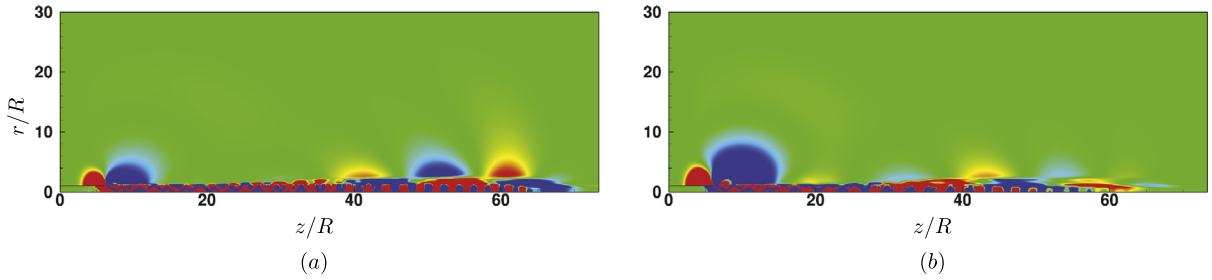
Fig. 14. Visualization of unstable eigenmodes showing Re($\hat{V}_z$) for (a) $\alpha = 2.0$ and (b) $\alpha = 4.0$ with contour levels $|\hat{V}_z/c_\infty| \leq 10^{-4}$.
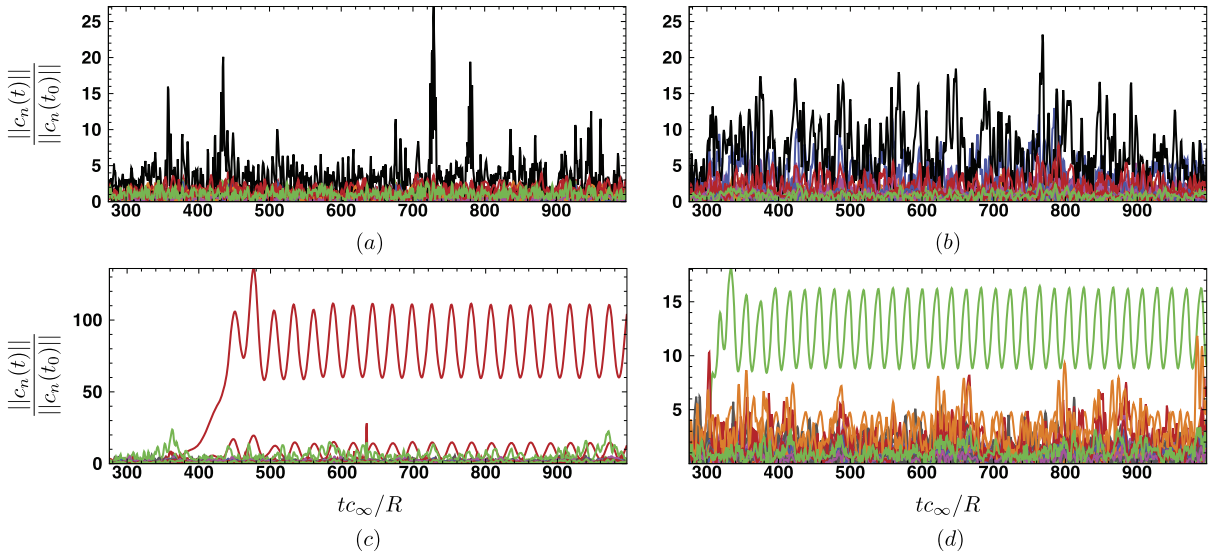

Fig. 15. Projection of the flow perturbations onto the global modes for all the flows for the eigenvalues shown in Fig. 13: (a) $\alpha = -2.0$, (b) no control, (c) $\alpha = 2.0$, and (d) $\alpha = 4.0$.
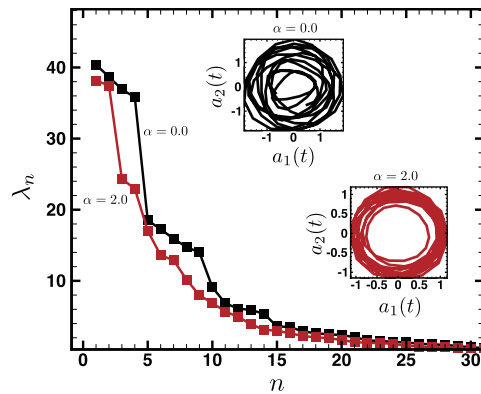

Fig. 16. POD eigenvalues and projection coefficients for the uncontrolled (flow L1, $\alpha = 0.0$) and controlled (flow L2, $\alpha = 2.0$) jets.

cally important. A proper orthogonal decomposition of the flow field using the pressure semi-norm confirms that the quieter flows are more regular (see Fig. 16), with less vigorous vortex pairing in a manner similar to that found by Wei and Freund [54] for optimal control of a two-dimensional mixing layer. Additional POD details, including its application to jets L3 and L4, may be found in Natarajan [31].

Although the appearance of the low-frequency, hydrodynamically-bound unstable global mode does not seem to have been reported on in the literature, the axisymmetric jet assumption leaves open the possibility that it is not relevant for turbulent jets. We thus apply our jet noise reduction approach to a Mach 0.9 turbulent jet.

Table 3
Simulation parameters for the turbulent jet.

Domain size	Cartesian grid
	$(L_x, L_y, L_z) = (0.25D, 0.25D, 30D)$
	Cylindrical grid
	$(r_{\min}, r_{\max}, L_z) = (0.25D, 12.5D, 30D)$
Grid points	Cartesian grid
	$(N_x, N_y, N_z) = (50, 50, 459)$
	Cylindrical grid
	$(N_r, N_\theta, N_z) = (318, 32, 459)$
Nozzle length	$L_{\text{nozzle}}/D = 3$
Nozzle thickness	$t_{\text{nozzle}}/D = 0.025$
Reynolds number	$\rho_j U_j D / \mu_j = 88{,}000$
Mach number	$U_j / c_j = 0.9$
Temperature ratio	$T_j / T_\infty = 0.6$
Nozzle wall temperature	$T_w / T_\infty = 1$
Momentum thickness at nozzle exit	$\theta/D = 0.03$
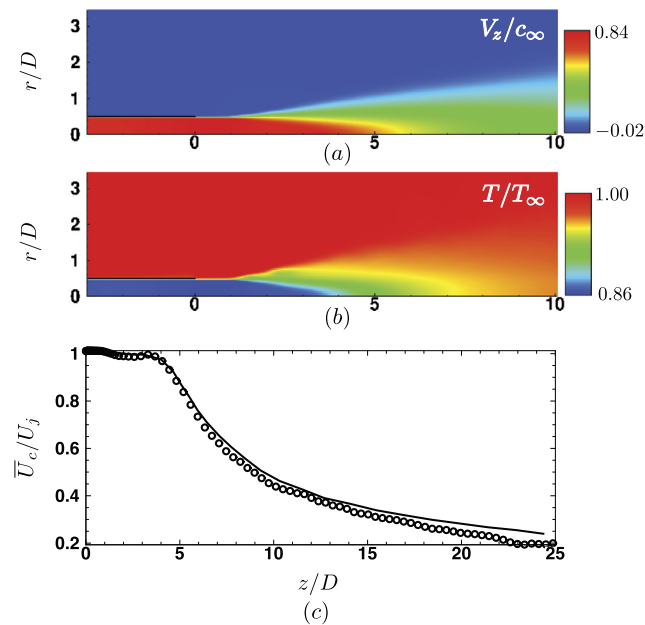
Fig. 17. Time-and-azimuthal averaged contours of (a) axial velocity and (b) temperature; (c) centerline axial velocity: present (—); Bodony & Lele [56] (○).

## 4. Noise reduction of a turbulent jet

4.1. Flow solution

The Mach-0.9 cold jet shown in Fig. 1(b) was simulated using the methods described in Section 2.2 and is the same as the large-eddy simulation implementation of Kim et al. [55]. The simulation parameters used are given in Table 3. An overset grid approach, also described in Kim et al. [55], is used for the simulations with 5.81 million grid points. The grid consists of a Cartesian core grid $(L_x, L_y, L_z) = (0.25, 0.25, 30)D$ of dimensions $(N_x, N_y, N_z) = (50, 50, 459)$ and an outer annular cylindrical grid $(r_{\min}, r_{\max}, L_z) = (0.25, 12.5, 30)D$ of dimensions $(N_r, N_\theta, N_z) = (318, 32, 459)$. The target surface Ω for the computation of the near-field sound is cylindrical with radius $7D$.

4.2. Controller development using global modes

The baseflow for the global mode analysis is the time-and-azimuthal averaged flow averaged over $\Delta t\, c_\infty/D \sim 300$. Figs. 17(a–b) show the contours of axial velocity and temperature for the time-and-azimuthal averaged baseflow. (The axisymmetric jet time-averaged baseflow shown in Fig. 2 is quantitatively different from the turbulent jet baseflow.) Fig. 17(c) shows a comparison of the centerline axial velocity to the result of Bodony & Lele [56], who performed an LES of a jet at the same conditions but without a nozzle. From these and other mean flow properties [31] we conclude that the LES database is sufficiently realistic for our purposes.
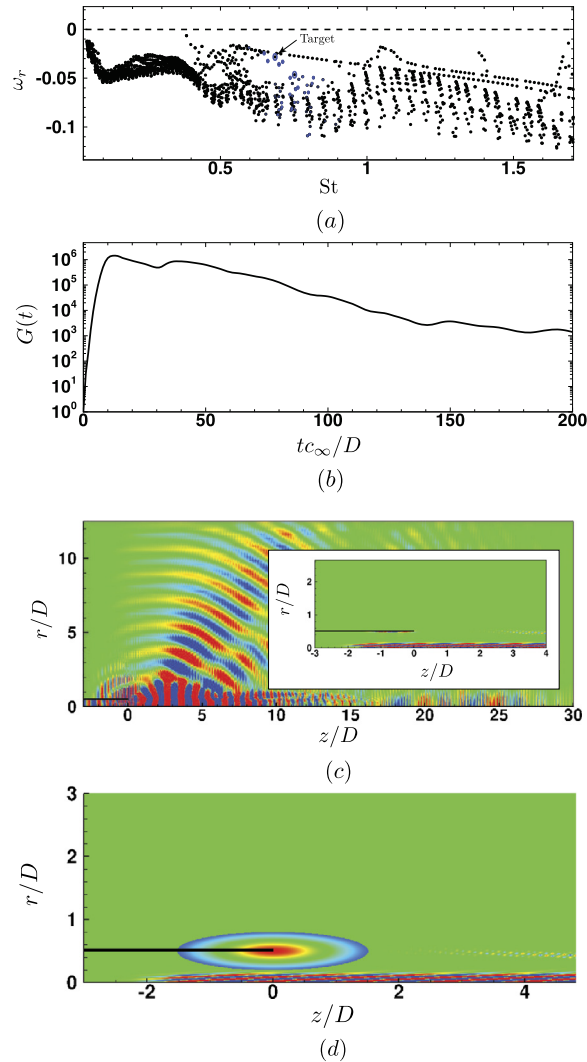
Fig. 18. (a) Eigenspectrum showing the mode contribution to the optimal initial condition corresponding to the maximum transient response in (b). The dominant transient growth mode ($\mathrm{Re}(\hat{p})$), identified as 'Target' in (a), is shown in (c) with contours $|\mathrm{Re}(\hat{p})/(\rho_\infty c_\infty^2)| \leq 10^{-6}$ and its adjoint ($\mathrm{Re}(\hat{V}_z^\dagger)$) with contour levels between $\pm 10^{-4}c_\infty$. The best co-located control region for the V_z (control) with V_r (feedback) controller is shown in (d).

It is understood that the $m = 0$ modes are an important component of even high-Reynolds-number turbulent jets [26], and previous studies of jet noise control suggest that disruption of the coherence of acoustically efficient axisymmetric flow structures is a possible approach [55] for noise reduction. Hence we focus on the axisymmetric modes for noise control in the present work. The spectrum for the time-and-azimuthal averaged flow for a wide range of Strouhal numbers ($St \sim 0.05$–1.70) is shown in Fig. 18(a). Previous studies, including Nichols and Lele [18], Nichols and Jovanovic [57], Schmidt et al. [58], have examined global mode spectra and the reader is referred to those references for more detailed analyses. Because our focus is on jet noise reduction, we construct the optimal transient response in Fig. 18(b), with leading forward and (inset) adjoint modes in Fig. 18(c). As anticipated, the adjoint mode contains grid oscillations arising from the discrete adjoint operator [42]. Using the controller optimization method described in Section 3.4.2 with the pressure-based semi-norm of Eq. (8), we determine that the best feedback controller actuates the axial momentum by sensing the radial velocity very near the nozzle lip, as shown in Fig. 18(d), to stabilize the eigenmode shown in Fig. 18(a) that most contributes to the jet's maximal optimal transient response. The best control matrix $\boldsymbol{C}$ is given by Eq. (11) with $\tilde{\boldsymbol{C}}^*$ indicating axial momentum forcing and radial momentum sensing and with the optimal parameters were found to be $(r_0^*, z_0^*, \ell_r^*, \ell_z^*) = (0.5, 0.0, 0.2, 1.0)D$. It is noteworthy that again it is found that the optimal controller senses the radial velocity and actuates the axial velocity. It is noteworthy that the turbulent jet meanflow suggests the same controller as found for the axisymmetric Mach-1.5 jet, with the former located slightly upstream and towards nozzle centerline relative to the latter (see Fig. 7(d)).
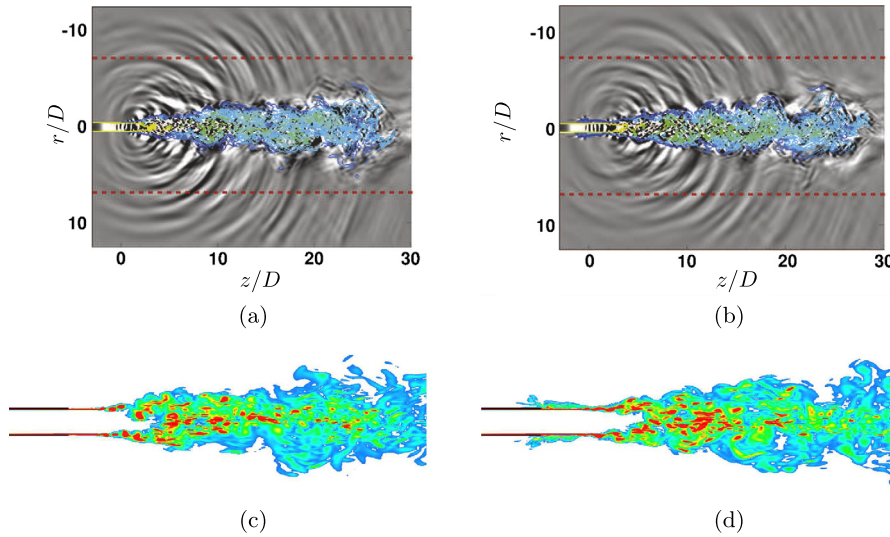
Fig. 19. Vorticity-dilatation contours for (a) baseline T1 and the (b) controlled flow T2 at $tc_\infty/D = 163$; near-nozzle view of vorticity contours for (c) baseline and (d) controlled flows at $tc_\infty/D = 163$.
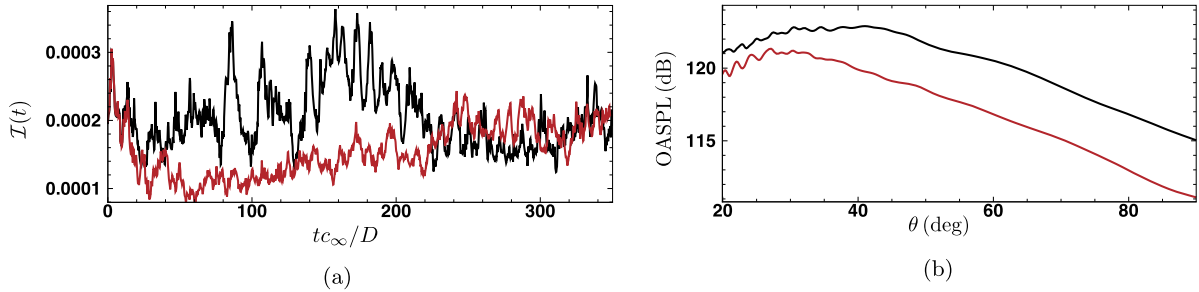

Fig. 20. (a) Measurement function $\mathcal{I}(t)$ and (b) overall sound pressure level on the target surface for the baseline (–) and controlled flows (–).

4.3. Noise controlled jet and its analysis

Using the control strategy in Section 4.2, we implemented the V_z (control)-V_r (feedback) controller as part of the LES calculation of the Mach-0.9 cold jet. To assess the performance of the control on the radiated sound of the baseline jet (T1), a LES was performed with a control gain of $\alpha = 2.0$ (T2). Figs. 19(a) and (b) show the instantaneous contours of vorticity-dilatation at $tc_\infty/D = 163$ for the baseline and T2 jets. The dilatation contours are less intense at the target surface for T2, which is indicative of its quieter nature. A near-nozzle view of the vorticity contours (Figs. 19(c) and (d)) show that, for the quieter flow, there is an enhancement of vorticity close to the nozzle lip.

To quantify the radiated sound, we compute the noise measurement function in Eq. (14) where Ω is the cylindrical target surface at $r_{target}/D = 7$. Fig. 20(a) shows the comparison of the noise objective function $\mathcal{I}(t)$ for the baseline (T1) and controlled flows. For the quieter jet, the controller has been effective in reducing the noise over a time interval of about $\Delta tc_\infty/D = 350$. The controlled jet lacks the intermittent, loud periods of time observed in turbulent jets. The controller impact on $\mathcal{I}(t)$ during the loud period $80 \leq tc_\infty/D \leq 220$ is greater than it is for $tc_\infty/D > 220$, similar to earlier work on optimal jet noise reduction [55]. Importantly, however, the controller also does not adversely raise the jet's radiated sound during the quiet period $tc_\infty/D > 220$. Fig. 20(b) shows the time-and-azimuthal averaged OASPL for the baseline and controlled flows at the target surface Ω. The angle θ is measured from the downstream jet axis along a line connecting the nozzle exit to the target surface. The quieter flow shows a consistent reduction of 3–4 dB for all angles $> 40°$ with a maximum reduction of approximately 4 dB at $90°$.

Using the axisymmetric Mach-1.5 jet results as a guide, we compute the spectrum of the time-and-azimuthally averaged baseflow for the controlled jet T2. As Fig. 21(a) shows, the control has modified the baseflow to allow for an unstable global mode of very low frequency, here around $St = 0.045$, whose structure is localized within the hydrodynamic region of jet (Fig. 21(b)). This hydrodynamically-bound mode appears to be of the type H modes found for the axisymmetric jet. The targeted eigenvalues move qualitatively similar to the axisymmetric Mach-1.5 jet (see Fig. 12) and are thus not explicitly shown; the controlled jet transient growth is also not shown because the unstable mode dominates the response for timescales $Tc_\infty/R \approx 44$.
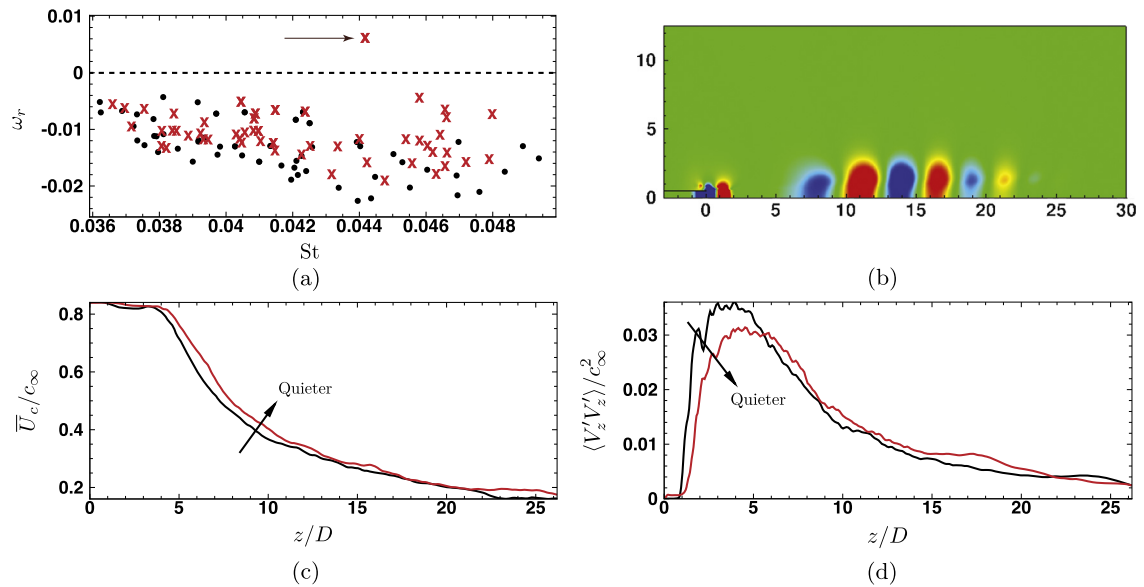
Fig. 21. (a) Eigenspectrum comparison for the baseline (•) and controlled (×) time-and-azimuthal averaged flows at low Strouhal numbers. (b) Unstable eigenmode (Real($\hat{p}$)) for the controlled flow showing non-radiative structure using contour levels between $\pm 10^{-4} \rho_\infty c_\infty^2$. Effects of control on (c) centerline axial velocity and (d) the mean square of axial velocity fluctuations along the jet lip line.

The mean flow of the controlled Mach-0.9 jet shows a reduction in mean flow acceleration and corresponding reduction in the lip-line axial velocity fluctuations, as shown in Figs. 21(c) and (d), respectively. The controlled jet shows a reduced near-nozzle reduction in the axial velocity, between $1 \leq z/D \leq 5$, which was discussed in Bodony and Lele [59] to be associated with a reduced axial coherence of disturbances exiting the nozzle and, ultimately, to a quieter jet.

5. Discussion

Through simulations of two high-speed jets—one axisymmetric and Mach 1.5 and another turbulent and Mach 0.9—a global mode-based control designed to stabilize the global mode that most contributes to transient growth, noise reductions have been realized using linear feedback controllers. In both jets the control targeted modes with frequency around $St \approx 0.5$; however, the resulting time-averaged baseflows supported one unstable mode (for the parameter range studied) with frequency closer to $St \approx 0.05$, roughly 1/10th that of the targeted mode. These low-frequency modes do not appear to have been discussed in the literature but they seem central to jet noise reduction in this effort. The modes appear to be of a new type, so-called type H, which are hydrodynamically bound to the jet without a significant acoustic field.

It seems that these low-frequency modes collect fluctuations onto less acoustically efficient motions. How these modes are generated and how the baseflow is modified by the higher-frequency forcing are not yet known, but other studies, such as by Samimy et al. [60], have found that forcing at frequencies higher than the acoustically-dominant $St = 0.3$ frequency appear to reduce a jet's radiated noise at near-sonic Mach numbers. Jordan and Colonius [1] summarize examples where changing the jet's low frequency dynamics can also affect its radiated noise. It is possible that a means to reduce jet noise could be to alter its low-frequency modes, either directly through control or indirectly through baseflow modification.

6. Conclusions

A global mode-based approach to developing linear feedback controllers is used to reduce the noise radiated from high-speed jets. Using a componentwise structural sensitivity analysis, actuator selection and placement is quantified based upon eigenvalue movement. The present study targets the dominant transient growth modes, with frequency $St \approx 0.5$, where it is found that axial momentum forcing using radial velocity sensing located near the nozzle lip, is the preferred actuator for the two cold near-sonic jets considered. The control is demonstrated first on an axisymmetric Mach-1.5 cold jet issuing from a cylindrical constant temperature nozzle, for which it reduces the jet's unsteady velocity fluctuation levels within the hydrodynamic region as well as the radiated noise. Reductions between 2 and 5 dB are observed, depending on observer angle. The control seems to work by exciting a low-frequency ($St \approx 0.05$) unstable mode that is dynamically important. It is hypothesized that this low-frequency mode, which lacks an extensive acoustic field (and labeled Type H), redistributes the fluctuations onto less acoustically-efficient motions. These conclusions are found to also apply for the turbulent Mach-0.9 jet, where an unstable Type-H mode is created by the baseflow modification and the jet's overall noise is also reduced by 1–4 dB.

References

[1] P. Jordan, T. Colonius, Wave packets and turbulent jet noise, Annu. Rev. Fluid Mech. 45 (2013) 173–195.
[2] C.K.W. Tam, P.J. Morris, The radiation of sound by the instability waves of a compressible plane turbulent shear layer, J. Fluid Mech. 98 (1980) 349–381.
[3] C.K.W. Tam, D.E. Burton, Sound generated by instability waves of supersonic flows. Part 1. Two-dimensional mixing layers, J. Fluid Mech. 138 (1984) 249–271.
[4] C.K.W. Tam, D.E. Burton, Sound generated by instability waves of supersonic flows. Part 2. Axisymmetric jets, J. Fluid Mech. 138 (1984) 273–295.
[5] A. Michalke, Survey on jet instability theory, Prog. Aerosp. Sci. 21 (1984) 159–199.
[6] C.K. Tam, F.Q. Hu, On the three families of instability waves of high-speed jets, J. Fluid Mech. 201 (1989) 447–483.
[7] M.E. Goldstein, S. Leib, The role of instability waves in predicting jet noise, J. Fluid Mech. 525 (2005) 37–72.
[8] A. Samanta, J.B. Freund, Finite-wavelength scattering of incident vorticity and acoustic waves at a shrouded-jet exit, J. Fluid Mech. 612 (2008) 407–438.
[9] A. Samanta, J.B. Freund, A model supersonic buried-nozzle jet: instability and acoustic wave scattering and the far-field sound, J. Fluid Mech. 778 (2015).
[10] T. Suzuki, T. Colonius, Instability waves in a subsonic round jet detected using a near-field phased microphone array, J. Fluid Mech. 565 (2006) 197–226.
[11] K. Gudmundsson, T. Colonius, Parabolized Stability Equation Models for Turbulent Jets and Their Radiated Sound, AIAA Paper 2009-3380, 2009.
[12] A. Sinha, D. Rodríguez, G.A. Brès, T. Colonius, Wavepacket models for supersonic jet noise, J. Fluid Mech. 742 (2014) 71–95.
[13] P. Balakumar, Prediction of Supersonic Jet Noise, AIAA Paper 98-1057, 1998.
[14] C. Yen, N. Messersmith, The Use of Compressible Parabolized Stability Equations for Prediction of Jet Instabilities and Noise, AIAA Paper 99-1859, 1999.
[15] L.C. Cheung, D.J. Bodony, S.K. Lele, Noise Radiation Predictions from Jet Instability Waves Using a Hybrid Nonlinear PSE-Acoustic Analogy, AIAA Paper 2007-3638, Presented at the 13th AIAA/CEAS Aeroacoustics Conference, Rome, Italy, 2007.
[16] V. Theofilis, Global linear instability, Annu. Rev. Fluid Mech. 43 (2011) 319–352.
[17] V. Theofilis, T. Colonius, Special issue on global flow instability and control, Theor. Comput. Fluid Dyn. 25 (2011) 1–6.
[18] J.W. Nichols, S.K. Lele, Global modes and transient response of a cold supersonic jet, J. Fluid Mech. 669 (2011) 225–241.
[19] X. Garnaud, L. Lesshafft, P. Schmid, P. Huerre, Modal and transient dynamics of jet flows, Phys. Fluids (1994–present) 25 (2013) 044103.
[20] W. Coenen, L. Lesshafft, X. Garnaud, A. Sevilla, Global instability of low-density jets, J. Fluid Mech. 820 (2017) 187–207.
[21] O. Semeraro, L. Lesshafft, V. Jaunet, P. Jordan, Modeling of coherent structures in a turbulent jet as global linear instability wavepackets: theory and experiment, Int. J. Heat Fluid Flow 62 (2016) 24–32 (Part A).
[22] J. Chomaz, Global instabilities in spatially developing flows: non-normality and nonlinearity, Annu. Rev. Fluid Mech. 37 (2005) 357–392.
[23] F. Giannetti, P. Luchini, Structural sensitivity of the first instability of the cylinder wake, J. Fluid Mech. 581 (2007) 167–197.
[24] D.J. Bodony, M. Natarajan, Controller selection and placement in compressible turbulent flows, in: Proceedings of the Summer Program, Center for Turbulence Research, 2012, pp. 35–42.
[25] M. Natarajan, J.B. Freund, D.J. Bodony, Actuator selection and placement for localized feedback flow control, J. Fluid Mech. 809 (2016) 775–792.
[26] A.V. Cavalieri, D. Rodríguez, P. Jordan, T. Colonius, Y. Gervais, Wavepackets in the velocity field of turbulent jets, J. Fluid Mech. 730 (2013) 559–592.
[27] M.R. Visbal, D.V. Gaitonde, On the use of higher-order finite-difference schemes on curvilinear and deforming meshes, J. Comput. Phys. 181 (2002) 155–185.
[28] J. Freund, Proposed inflow/outflow boundary condition for direct computation of aerodynamic sound, AIAA J. 35 (1997) 740–742.
[29] D.J. Bodony, Analysis of sponge zones for computational fluid mechanics, J. Comput. Phys. 212 (2006) 681–702.
[30] H.R. Lewis, P.M. Bellan, Physical constraints on the coefficients of Fourier expansions in cylindrical coordinates, J. Math. Phys. 31 (1990) 2592–2596.
[31] M. Natarajan, Actuator Selection and Placement for Linear Feedback Control of Compressible Flows, Ph.D. thesis, University of Illinois at Urbana–Champaign, IL, USA, 2017.
[32] B. Strand, Summation by parts for finite difference approximations for d/dx, J. Comput. Phys. 110 (1994) 47–67.
[33] P. Moin, K. Squires, W. Cabot, S. Lee, A dynamic subgrid-scale model for compressible turbulence and scalar transport, Phys. Fluids A, Fluid Dyn. (1989–1993) 3 (1991) 2746–2757.
[34] D.K. Lilly, A proposed modification of the Germano subgrid-scale closure method, Phys. Fluids A, Fluid Dyn. 4 (1992) 633–635.
[35] E.T. Spyropoulos, G.A. Blaisdell, Evaluation of the dynamic model for simulations of compressible decaying isotropic turbulence, AIAA J. 34 (1996) 990–998.
[36] S.K. Lele, Compact finite difference schemes with spectral-like resolution, J. Comput. Phys. 103 (1992) 16–42.
[37] S. Kawai, S.K. Shankar, S.K. Lele, Assessment of localized artificial diffusivity scheme for large-eddy simulation of compressible turbulent flows, J. Comput. Phys. 229 (2010) 1739–1762.
[38] M. Svärd, M. Carpenter, J. Nordström, A stable high-order finite difference scheme for the compressible Navier–Stokes equations, far-field boundary conditions, J. Comput. Phys. 225 (2007) 1020–1038.
[39] M. Svärd, J. Nordström, A stable high-order finite difference scheme for the compressible Navier–Stokes equations: no-slip wall boundary conditions, J. Comput. Phys. 227 (2008) 4805–4824.
[40] K. Mattsson, M. Svärd, M. Shoeybi, Stable and accurate schemes for the compressible Navier–Stokes equations, J. Comput. Phys. 227 (2008) 2293–2316.
[41] D. Bodony, Accuracy of the simultaneous-approximation-term boundary condition for time-dependent problems, J. Sci. Comput. 43 (2010) 118–133.
[42] G.J. Chandler, M.P. Juniper, J.W. Nichols, P.J. Schmid, Adjoint algorithms for the Navier–Stokes equations in the low Mach number limit, J. Comput. Phys. 231 (2012) 1900–1916.
[43] S. Balay, J. Brown, K. Buschelman, W.D. Gropp, D. Kaushik, M.G. Knepley, L.C. McInnes, B.F. Smith, H. Zhang, PETSc Web page, http://www.mcs.anl.gov/petsc, 2012.
[44] S. Balay, J. Brown, K. Buschelman, V. Eijkhout, W.D. Gropp, D. Kaushik, M.G. Knepley, L.C. McInnes, B.F. Smith, H. Zhang, PETSc Users Manual, Technical Report ANL-95/11 – Revision 3.3, Argonne National Laboratory, 2012.
[45] S. Balay, W.D. Gropp, L.C. McInnes, B.F. Smith, Efficient management of parallelism in object oriented numerical software libraries, in: E. Arge, A.M. Bruaset, H.P. Langtangen (Eds.), Modern Software Tools in Scientific Computing, Birkhäuser Press, 1997, pp. 163–202.
[46] V. Hernandez, J.E. Roman, V. Vidal, SLEPc: a scalable and flexible toolkit for the solution of eigenvalue problems, ACM Trans. Math. Softw. 31 (2005) 351–362.
[47] P. Amestoy, I. Duff, J. L'Excellent, J. Koster, Mumps: a general purpose distributed memory sparse solver, in: Applied Parallel Computing. New Paradigms for HPC in Industry and Academia, 2001, pp. 121–130.
[48] E. Åkervik, L. Brandt, D. Henningson, J. Hœpffner, O. Marxen, P. Schlatter, Steady solutions of the Navier–Stokes equations by selective frequency damping, Phys. Fluids 18 (2006) 068102.
[49] D. Hammond, L. Redekopp, Global dynamics of symmetric and asymmetric wakes, J. Fluid Mech. 331 (1997) 231–260.
[50] D. Sipp, A. Lebedev, Global stability of base and mean flows: a general approach and its applications to cylinder and open cavity flows, J. Fluid Mech. 593 (2007) 333–358.
[51] P.J. Schmid, D.S. Henningson, Stability and Transition in Shear Flows, vol. 142, Springer Science & Business Media, 2012.
[52] J. Nichols, S. Lele, P. Moin, Global mode decomposition of supersonic jet noise, in: Annual Research Briefs, Center for Turbulence Research, Stanford, CA, 2009, pp. 3–15.

[53] S.-P. Han, A globally convergent method for nonlinear programming, J. Optim. Theory Appl. 22 (1977) 297–309.
[54] M. Wei, J.B. Freund, A noise-controlled free shear flow, J. Fluid Mech. 546 (2006) 123–152.
[55] J. Kim, D.J. Bodony, J.B. Freund, Adjoint-based control of loud events in a turbulent jet, J. Fluid Mech. 741 (2014) 28–59.
[56] D.J. Bodony, S.K. Lele, On using large-eddy simulation for the prediction of noise from cold and heated turbulent jets, Phys. Fluids (1994–present) 17 (2005) 085103.
[57] J. Nichols, M. Jovanovic, Input–output analysis of high-speed jet noise, in: Proceedings of the Summer Program, Center for Turbulence Research, 2014, p. 251.
[58] O. Schmidt, A. Towne, T. Colonius, P. Jordan, V. Jaunet, A.V. Cavalieri, G.A. Brès, Super- and multi-directive acoustic radiation by linear global modes of a turbulent jet, in: 22nd AIAA/CEAS Aeroacoustics Conference, 2016, p. 2808.
[59] D.J. Bodony, S.K. Lele, Current status of jet noise predictions using large-eddy simulation, AIAA J. 46 (2008) 364–380.
[60] M. Samimy, J.-H. Kim, J. Kastner, I. Adamovich, Y. Utkin, Active control of a Mach 0.9 jet for noise mitigation using plasma actuators, AIAA J. 45 (2007) 890–901.